Fabrication of Low Loss Lithium Niobate Rib Waveguides Through Photoresist Reflow

Karan Prabhakar and Ronald M. Reano

Abstract—We present lithography and argon plasma etching of lithium niobate on insulator (LNOI) rib waveguides using reflowed photoresist etch masks and 405 nm photolithography. Melting the photoresist at temperatures greatly exceeding its glass transition temperature while minimizing feature distortion through photoresist adhesion control reduces sidewall surface roughness and allows the photoresist to be used both as the pattern mask and the hard etch mask. Waveguide sidewall surfaces exhibiting sub-nm root mean square roughness are fabricated. Dependence of sidewall roughness and angle on feature width, and propagation loss on thermal annealing of the fabricated devices is characterized. Measured quality factors on fabricated microresonators exceed one million. LNOI rib waveguides and resonators with low propagation loss increase nonlinear optical conversion efficiencies and are useful for efficient electro-optic modulation. Photolithography compatible fabrication of low loss LNOI photonic integrated circuits facilitates scalable commercialization.

Index Terms—Lithium niobate, lithium niobate on insulator (LNOI), microresonators, photonic integrated circuits, waveguides.

I. Introduction

ITHIUM niobate (LN) is a nonlinear optical material widely used for applications in optical frequency conversion, optical modulation, and quantum information science. The thin film lithium niobate on insulator (LNOI) platform has seen extensive use over the past decade to demonstrate compact onchip devices such as second harmonic generators, optical parametric oscillators, electro-optical modulators, entangled photon sources, and frequency combs [1], [2], [3], [4], [5], [6], [7], [8], [9], [10], [11], [12]. Systems utilizing LN benefit from the wide transparency range of the material which spans from ultraviolet to mid infrared [13]. On chip integrated LNOI waveguides enable efficient nonlinear optical conversion by virtue of high modal field overlap between interacting optical modes [3]. Large optical intensities inside these waveguides can be obtained with low powers as optical mode sizes of less than 1 μ m² are possible on the LNOI platform. Moreover, electro-optical modulators can be designed with a high overlap of the interacting microwave and optical modes allowing for operation of these devices at low voltages [5], [7]. The ability to fabricate thin film LNOI on

Manuscript received 18 September 2022; revised 6 November 2022; accepted 10 November 2022. Date of publication 15 November 2022; date of current version 24 November 2022. This work was supported by the National Science Foundation under Award 1809894. (Corresponding author: Karan Prabhakar.)

The authors are with the ElectroScience Laboratory, Department of Electrical and Computer Engineering, The Ohio State University, Columbus, OH 43212 USA (e-mail: prabhakar.25@osu.edu; reano.1@osu.edu).

Digital Object Identifier 10.1109/JPHOT.2022.3222184

silicon substrates has also opened avenues for hybrid integration of electronic and optical devices [14], [15], [16].

On-chip LNOI waveguides primarily utilize strip loading or etched rib structures for optical waveguiding. Strip loading with a similar refractive index material such as silicon nitride allows for defining waveguides without etching the LN [17], [18], [19]. However, this results in a fraction of the optical modal power to reside in the strip material which lowers optical conversion efficiencies in processes that benefit from the optical nonlinearity of LN, while requiring the deposition and etching of the strip material. Moreover, LNOI strip loaded waveguides can produce excess propagation loss if the strip material has higher optical absorption than LN. Rib waveguides, on the other hand, allow efficient nonlinear processes but require smooth etched sidewalls for low scattering losses.

The primary source of optical propagation loss in LN rib waveguides is attributed to optical scattering by rough etched sidewalls. Etching rib waveguiding structures in LN is a challenging process. Wet etching using HF and HNO₃ can be used to pattern waveguides, but due to the anisotropic etching rates along different crystal axis wet etching is best suited to Z-cut films, since the highest etching rate is along the crystal Z-axis [20]. Reactive ion etching (RIE) based processes are suited to all crystal orientations, however, using fluorine and chlorine based etch chemistries leads to excess roughness due to reaction byproduct redeposition which is difficult to remove using chemical cleaning [21]. Physical etching processes, such as Ar plasma etching and chemical mechanical polishing (CMP), have been shown to achieve the lowest sidewall roughness as redeposited material can be removed.

To date, waveguide patterning techniques to fabricate low loss LNOI waveguides include electron beam lithography (EBL) with electron beam resists followed by Ar plasma etching [22], [23], focused ion beam (FIB) lithography [24], CMP [25], [26], [27], and photolithography assisted chemical mechanical etching (PLACE) [28], [29], [30]. While methods such as EBL followed by Ar plasma etching, or FIB, can produce low sidewall roughness, they are less suited for full wafer patterning due to sequential writing. CMP processing also results in smooth sidewalls, however, when compared to plasma etching, CMP processes result in lower within-wafer and wafer-to-wafer film etching uniformity [31].

EBL, CMP, PLACE, and photolithography require metal masks or hard etch masks, such as Si and SiO₂ [32], [33]. These masks improve etch or polish selectivity since physical etching processes like CMP and Ar plasma etching show little material

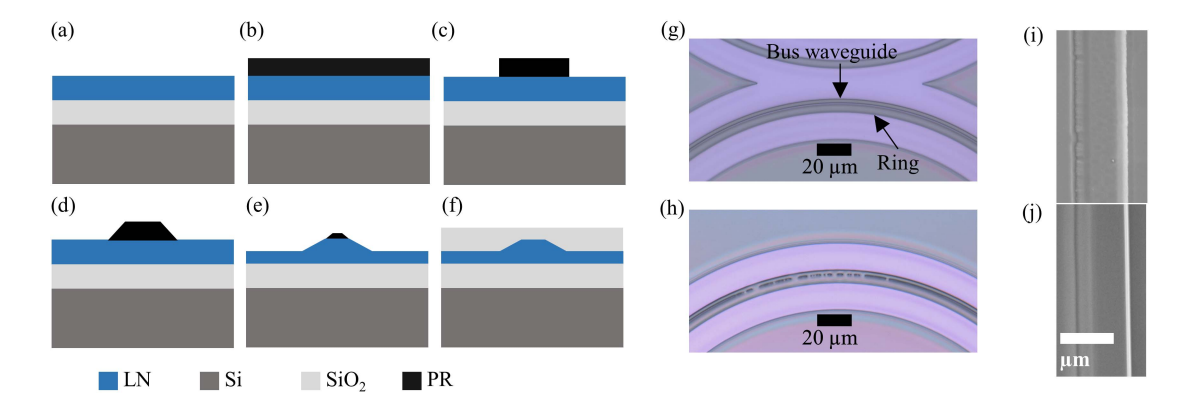


Fig. 1. Fabrication of LN rib waveguides using photoresist reflow. (a) clean and HMDS prime of substrate, (b) spin coat of PR, (c) exposure and development followed by O2 plasma ashing, (d) reflow of PR at high temperature, (e) etch via Ar plasma etching, and (f) deposition of cladding. Optical micrograph of bus coupled ring resonator showing (g) restrained PR reflow resulting in clear definition of bus-ring gap, and (h) unrestrained PR reflow resulting in defects. SEM images of LN waveguides etched (i) without, and (j) with the reflowed PR showing improvement in sidewall roughness.

selectivity. The need for metal or hard etch mask layers increases processing steps while adding the possibility of material contamination, in particular metal contamination, on waveguides which can lead to excess losses.

While it has been demonstrated that high temperature photoresist (PR) reflow conducted inside a plasma environment can lead to an improvement in sidewall roughness when etching AlGaAs waveguides using RIE [34], it is unknown if a sufficient increase in PR hardness can be obtained to allow physical etching processes such as Ar plasma etching. PR reflow is also routinely used to fabricate smooth microlens arrays [35]. However, thermal PR reflow process to form microlens or waveguides is susceptible to boundary migration due to uncontrolled reflow leading to lateral spread of features.

In this work, we present an alternative waveguide patterning method using photolithography and high temperature photoresist reflow to plasma etch rib waveguides in LNOI with a positive tone PR mask. We demonstrate that high temperature melting of the PR, while mitigating the lateral spread of features using surface energy discontinuities on the LN surface, achieves sufficient increase in physical etching resistance and improvement in sidewall roughness to act as a hard mask. Our technique produces plasma etched surfaces with sub-nanometer root mean square (rms) roughness similar to those obtained via CMP and PLACE [25]. We also show that 405 nm h-line photolithography with a resolution limit of 0.5 µm is compatible with our methods. Measurements from ring and disc resonators fabricated using this technique show intrinsic and loaded quality factors (Q_I and Q_L, respectively) exceeding one million. The technique reduces the processing steps and method complexity while also being compatible with full wafer processing.

II. FABRICATION

The fabrication of the rib waveguides is conducted on commercial X-cut LNOI (NanoLN). The LN film, SiO_2 insulator, and Si handle substrate thicknesses are 400 nm, 4.7 μ m, and 500 μ m, respectively. For experiments, a 4" LNOI wafer is diced

into square substrates with side length of 1 cm. Fig. 1(a)–(f) shows the process flow for the fabrication of waveguides and resonators.

A. Lithography and Mask Definition

An LNOI substrate is initially cleaned using solvents and SC-1 solution (one-part NH₄OH, one-part H₂O₂, and five parts DI water). The substrate is then primed with a hexamethyldisilazane (HMDS) monolayer in a vacuum oven at 150 °C. Proper cleaning and uniform priming is important for defect free PR development and reflow. A PR (SPR-955 CM-0.9) layer of thickness 740 nm is spin-coated next. Rib waveguide patterns are exposed and developed on the substrate using a 405 nm pholithographic maskless aligner (Heidelberg MLA 150). A dose of 90 mJ/cm² was used for exposure and Microposit MF-CD-26 developer was used for development. The patterned PR features are subjected to low power (45 W) O₂ plasma ashing for 4 minutes to remove PR and HMDS residue and expose a clean LN surface on the bare regions of the sample. The O₂ plasma ashing only etches about 5 nm of the PR layer. Next, an optimized PR reflow is conducted in a N₂ ambient at 200 °C. The samples were loaded into an oven at 100 °C, ramped to 200 °C in 30 minutes, held at 200 °C for 10 minutes and ramped down to 100 °C in 30 minutes and unloaded. After the reflow, an 8% decrease in PR film thickness is observed. An illustration of the PR cross-section after the reflow is shown in Fig. 1(d).

A restrained and defect free PR reflowed mask for a ring resonator in a pulley style coupling configuration is shown in Fig. 1(g). The width of the coupling gap between the bus waveguide and the ring waveguide is 0.5 μ m as and appears as pink in color in the figure. Note, the resolution limit of our lithography is also 0.5 μ m. The bus waveguide width is 2.5 μ m and the ring resonator waveguide width is 5 μ m, both appearing grey in color in the figure. Multimode waveguides were fabricated to reduce interaction of the modal electric field with the sidewalls. Upon omitting the plasma ashing step, we observe defects in the coupling region due to the merger of the bus and ring waveguides as shown in Fig. 1(h). Low power plasma ashing in O₂ ambient

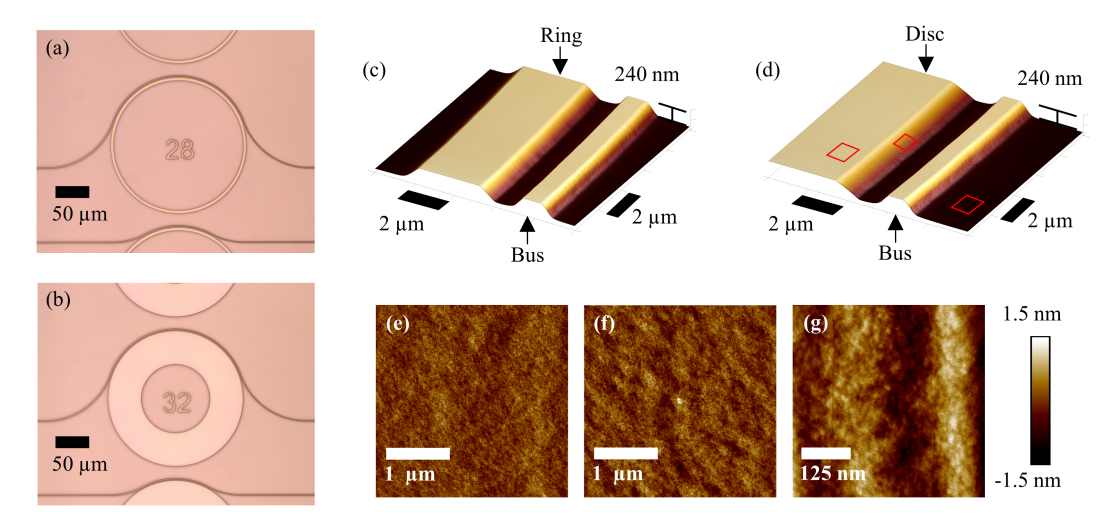


Fig. 2. Optical micrographs of fabricated (a) ring and (b) disc resonators. Perspective-view AFM scans of the (c) ring and (d) disc coupling regions showing smooth resonator sidewalls. Red boxes on the AFM scan denote unetched surface, etched sidewall, and etched surface from left to right. Top-view AFM scans of (e) unetched surface, (f) etched surface, and (g) etched sidewall surface with rms roughness of 0.26 nm, 0.30 nm, and 0.49 nm respectively.

removes residual PR and HMDS from the unpatterned regions of the LN surface restraining the reflow of PR features to within the patterned regions. In the absence of O₂ plasma ashing step, PR and HMDS residue between features that are closely spaced together causes features to merge during the high temperature reflow process since the viscous PR can bridge across the gap aided by residue. Along isolated waveguides, the residue can also lead to reflow that produces ripples along the mask, similar to undulations observed using thermal photoresist reflow methods for waveguides fabricated on AlGaAs substrates [34].

B. Waveguide Etching

The rib waveguides are defined using Ar plasma etching. The samples are etched in 5 mTorr pressure in an inductively coupled plasma – reactive ion etching (ICP-RIE) tool at 19 °C. The samples are cooled inside the tool using backside helium cooling. Argon flow rate of 50 SCCM is used. A bias power of 150 W and ICP power of 300 W is utilized, and a temperature of 19 °C is maintained. An LN etch rate of 30 nm/min was observed along with an etch rate of 57 nm/min for the reflowed PR. Without the reflow, the PR shows a higher etch rate of 71 nm/min. The LN thin film is etched to a depth of 240 nm to define the ribs. After Ar plasma etching, the residual PR cannot be removed using solvent cleaning, hence SC-1 cleaning at 70 °C for 60 minutes is needed to remove the PR residue completely. The samples are then finally cleaned in O2 plasma in an ICP-RIE tool at low power before deposition of 1.5 μm of silicon oxide (SiO_x) cladding using plasma enhanced chemical vapor deposition (PECVD). To allow edge coupling using lensed fibers for optical measurements, the sample edges are trimmed by dicing and polished using a mechanical polisher.

Ring resonators with radii 100 μ m and 150 μ m were fabricated using this process. Fig. 2(a), (b) show the fabricated ring resonators with radius 100 μ m and a rib waveguide base width of 5 μ m and 50 μ m, respectively. Resonators with the waveguide width of 50 μ m behave as disc resonators since they support

whispering gallery modes and are referred to as disc resonators in the remainder of the text.

For a given LN thin film thickness, the height of the waveguiding rib structure is an important parameter since weakly guided modes with low rib heights will cause excessive bend loss. Moreover, low rib heights can lead to an additional loss mechanism wherein the rib guided quasi-TE mode couples into a higher effective index slab TM mode [36]. Computational electromagnetic modeling using finite difference method shows that rib heights of 240 nm are sufficient to avoid excessive bending loss as well as slab mode coupling losses. Pulley-style evanescent field coupling excitation is chosen for the resonators since computational modeling shows that long coupling lengths are required at 1550 nm wavelength for 0.5 µm coupling gap.

C. Metrology and Fabrication Results

High temperature baking of the PR improves etch resistance to physical etching processes. For Ar plasma etching, the etch selectivity improves from 1:2.4 to 1:1.9 (LN:PR) indicating increased hardness, consistent with the observation of reduction in PR thickness with high temperature reflowing. During optimization of the PR reflow process, maximum temperatures are limited to 200 °C to avoid graphitization of the PR. SPR-955 is a cresol novolak polymer-based PR (note, the manufacturer recommendation for a hard bake is 120 °C). At temperatures of over 150 °C, organic polymer-based PR outgases H₂O, CO, and CO₂ which leads to an increase in the density of the film [37], however, higher temperatures may cause excessive graphitization through pyrolysis induced aromatization of the polymer [37], [38], [39], making removal of the PR residue after plasma etching challenging using SC-1. We also note that it has been demonstrated in literature that after high temperature baking at 220 °C, the PR can exhibit exceptional resistance to polishing processes such as CMP, even exceeding the polishing resistance of SiO₂ [40]. This implies that our process may also be used to pattern waveguides using CMP without requiring an additional

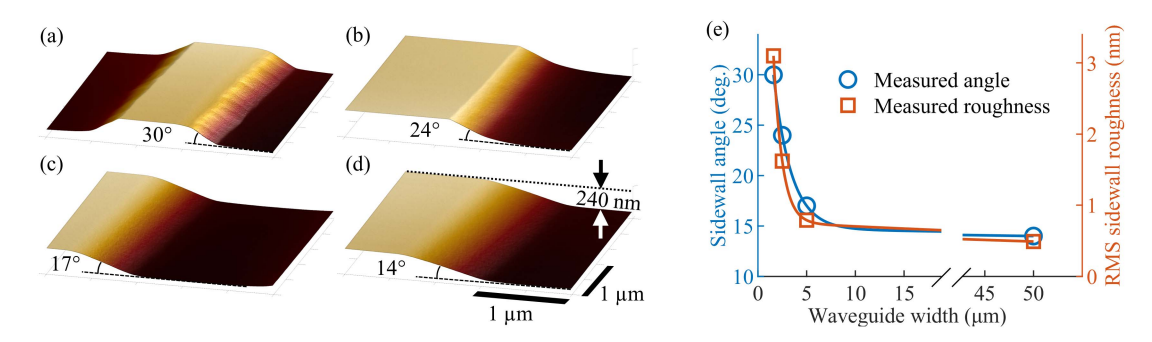


Fig. 3. AFM images showing LN rib sidewall profiles and angles for different waveguide rib widths. The rib widths are (a) $1.6 \mu m$, (b) $2.5 \mu m$, (c) $5 \mu m$, and (d) $50 \mu m$. (e) Measured dependence of sidewall angle and sidewall surface roughness on the waveguide width. Lines are exponential fits to data.

metal or a hard mask layer while solely relying on the reflowed PR as the polishing mask.

The PR reflow process at elevated temperatures is susceptible to boundary migration due to uncontrolled reflow [35]. Uncontrolled reflow may occur because of low mismatch of surface energies of the surface on which the PR is patterned and the surface devoid of any PR. In such cases, similar wettability is seen across the whole sample and the PR boundary can migrate with little change in free energy [41]. In our experiment, we introduce a discontinuity in the surface energies at the PR boundary. Since LN is mildly hydrophobic [42], and HMDS is an adhesion and wettability promoter for PR, by removing the residual HMDS layer and PR residue from the unpatterned regions using O₂ plasma treatment, a clean LN surface is exposed. As a result, upon high temperature PR reflow, the melted PR stays confined to the patterned regions on top of the HMDS layer to maintain the least amount of free energy and does not spread laterally.

Scanning electron microscopy (SEM) of the etched waveguides shows significant improvement in the sidewall roughness with the reflowed PR hard mask. Etched LN rib waveguides without and with the reflowed PR are shown in Fig. 1(i) and (j), respectively. Reduced sidewall roughness can be seen with the reflow. Surface characterization using atomic force microscopy (AFM) in Fig. 2(c)–(g) shows that smooth sidewalls and etched surfaces exhibiting sub-nm surface roughness are obtained using our process and sub-µm coupling gaps are clearly defined. The etched surface roughness is 0.30 nm [Fig. 2(f)], only a marginal increase from the unetched surface roughness of 0.26 nm [Fig. 2(e)] measured over an area of 3 μ m \times 3 μ m. Sloped sidewalls also allow direct measurement of surface roughness using AFM. A sidewall surface roughness of 0.49 nm is observed on the disc resonator sidewalls measured over an area of $0.5 \ \mu m \times 0.5 \ \mu m$.

We also observe different sidewall characteristics for different waveguide widths. Dependence of LN waveguide sidewall angle is characterized in Fig. 3. During the high temperature reflow process, the PR becomes flowable albeit viscous and possesses a characteristic surface tension. Contact angle of the viscous PR is therefore a function of the waveguide width leading to different sidewall angles upon hardening when cooled [43]. Highly sloped sidewalls are measured on larger feature widths and vice versa. Sidewall surface roughness is observed to decrease with

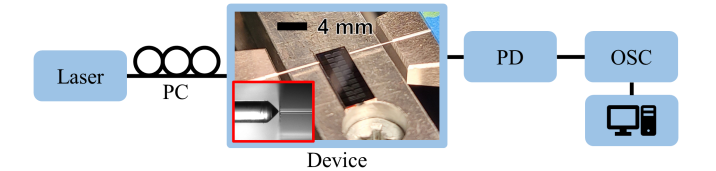


Fig. 4. Measurement setup showing the device chip on a stage with inset showing the fiber to chip coupling using lensed fibers.

increasing waveguide widths. Sidewall rms roughness of 0.49 nm on the 14° sidewall almost approaches that of the etched surface roughness while higher roughness is observed on waveguides with larger sidewall angles. As an additional design control parameter, the PR's surface tension may also be fine-tuned to obtain different sidewall angles.

III. OPTICAL CHARACTERIZATION

Optical measurements on the fabricated devices are conducted to characterize the Q factors and propagation loss. The measurement setup is shown in Fig. 4. Transmission response of the resonators is measured by sweeping the laser wavelength in time and recording the transmitted power via a photodiode on an oscilloscope. Upper limit of the propagation loss is found by using the measured FSR and fitting the resonance's wavelength dependent transmission data to the analytical transmission response for a resonator [44].

Thermal annealing of a fabricated ring resonator with radius 100 μm is conducted to study the change in Q_I, propagation loss, thermal budget, and optimum annealing temperature of the fabricated devices. The sample is annealed for 12 hours at different temperatures in an ambient air environment. Improvement in Q_I of the resonator is observed with increasing annealing temperatures up to 550 °C. Fig. 5(a) shows that $Q_{\rm I}$ can more than double the original value after annealing at 550 °C. We attribute this improvement in Q_I to the reduction in optical absorption by the silicon oxide cladding. At temperatures over 400 °C, it is known that hydrogen impurities outgas from SiO_x deposited using PECVD, thereby reducing the concentration of Si-H bonds and improving transmission [45]. Upon annealing at temperatures higher than 550 °C, Q_I is seen to reduce, and propagation loss increases. We believe that the increased film stress at these higher temperatures leads to nanometer-scale and

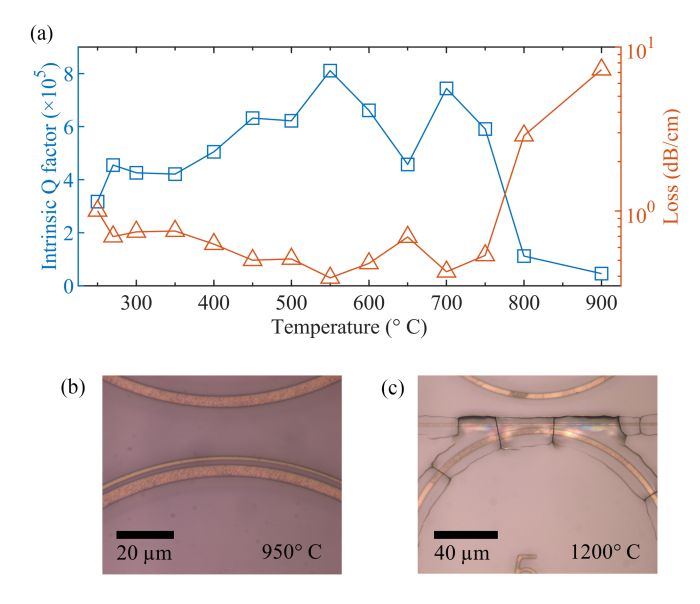


Fig. 5. (a) Effect of annealing temperature on quality factor and propagation loss of a ring resonator with 100 μm radius and 5 μm waveguide width. Optical micrographs of (b) microcracking of LN ribs at 950 °C and (c) cracking of SiO $_x$ cladding along the ribs at 1200 °C.

micrometer-scale cracks in the LN thin film devices thereby increasing optical scattering losses. At temperatures of over 900 °C, micrometer-scale cracking of the LN thin film devices is visible using an optical microscope as shown in Fig. 5(b). For annealing temperatures exceeding 950 °C, a spectral response from the devices can no longer be measured indicating catastrophic cracking of the devices. At an even higher temperature of 1200 °C, the $\rm SiO_x$ cladding along most of the waveguiding ribs is seen to crack as shown in Fig. 5(c). Thermal annealing of the fabricated resonator also reveals the devices may be used in temperatures of up to 550 °C without causing damage which can be useful to obtain phase matching in nonlinear optical processes over a large temperature range.

Microresonators with radius 150 µm annealed to 550 °C in an O₂ ambient exhibit the highest Q factors and lowest propagation loss. O₂ ambient was chosen to minimize film stress related microcracking on the devices since it been shown to improve stress stability of the SiO_x films deposited using PECVD [46]. Q_I and $Q_{\rm L}$ in excess of one million are measured on the resonators as shown in Fig. 6(c, d), which show the measured transmission spectrum around the resonances of the ring and disc resonator, respectively. A Q_I of 1.5×10^6 was measured (Q_L = 8.1×10^5) at 1557.31 nm, which corresponds to a propagation loss of 0.14 dB/cm (upper limit) on the ring resonator. FSR of 1.41 nm is measured for the ring mode from the spectral response shown in Fig. 6(a). On the disc resonators, a higher Q_I of 2.0×10^6 is measured ($Q_L = 1.1 \times 10^6$) at 1548.70 nm, which corresponds to a propagation loss of 0.11 dB/cm (upper limit). A FSR of 1.41 nm is measured for the disc from the spectral response shown in Fig. 6(b). While the resonators are multimode, we observe a consistent FSR in the resonators indicating that the same mode is present in the wavelength range of interest. Resonators were observed to be critically coupled at the points of measurement.

We also note that by over coupling the ring resonator using a cladding material with a slightly higher refractive index, broadband operation can be obtained with high resonance extinction ratios throughout the entire measured wavelength range as shown in Fig. 6(e). Broadband, almost single mode, operation is obtained for a ring resonator cladded with a PR (S1813) which exhibits a refractive index of approximately 1.60 at 1550 nm. Such a response is beneficial for uniform and high-quality multiwavelength switching and modulation in photonic networks [47]. Over coupled ring resonators have also been used to improve performance of add/drop filters and demonstrate fast light [48], [49], [50].

IV. RESULTS AND DISCUSSION

Process development, metrology, and optical measurements reveal that by using our method, we can fabricate smooth rib waveguiding structures with low propagation losses and resonators exhibiting Q_I of more than 10^6 using photolithography. By reflowing the PR at 200 °C, an Ar plasma etching selectivity of 1:1.9 (LN:PR) is obtained enabling sufficient rib etching depths. Surface AFM characterization shows that waveguides with a rib width of greater than 5 µm can be fabricated with sub-nm sidewall surface roughness. Resonators with 50 µm waveguide rib width show slightly better Q factors than resonators with 5 µm waveguide rib width. This is primarily because we measure lower sidewall surface roughness as waveguide width is increased. The sidewall angle can also be controlled by varying the feature width, useful for dispersion engineering. A further control over the waveguide's geometry, especially the sidewall angle may be obtained through tuning the PR's viscosity at high temperatures. We note, sloped sidewalls and methods to obtain different slopes have also been proposed using CMP by changing the polishing time [26]. Sidewall angles and etched sidewall surface roughness obtained using our process are very similar to those obtained using CMP or PLACE processes demonstrated on LN [25].

While Q factors more than 10⁶ are already sufficient for many applications on the LNOI platform, we believe that the propagation loss in our resonators is limited by the optical absorption in the SiO_x cladding layer deposited by PECVD. Significant E-field strength outside the 400 nm thick LN rib waveguides makes the propagation loss highly dependent on the cladding properties. This is indicated by the strong dependence of Q_I with thermal annealing due to improvement in the transmission of the SiO_x cladding. Uncladded resonators utilizing channel waveguides with similar sidewall angles and surface roughness can exhibit Q factors over 10⁷ [25]. We expect similar Q factors on our resonators without a cladding, translating to a magnitude of order lower propagation loss, however, limited by the lithography resolution of 0.5 µm, sufficient evanescent coupling between the bus and the resonators could not be established on uncladded resonators. Deep ultraviolet lithography may be used in the future to remove this limitation on the resolution and reduce the coupling gap. As demonstrated, while thermal annealing at 550 °C can increase the Q factors more than two-fold, researchers have shown that even higher temperatures

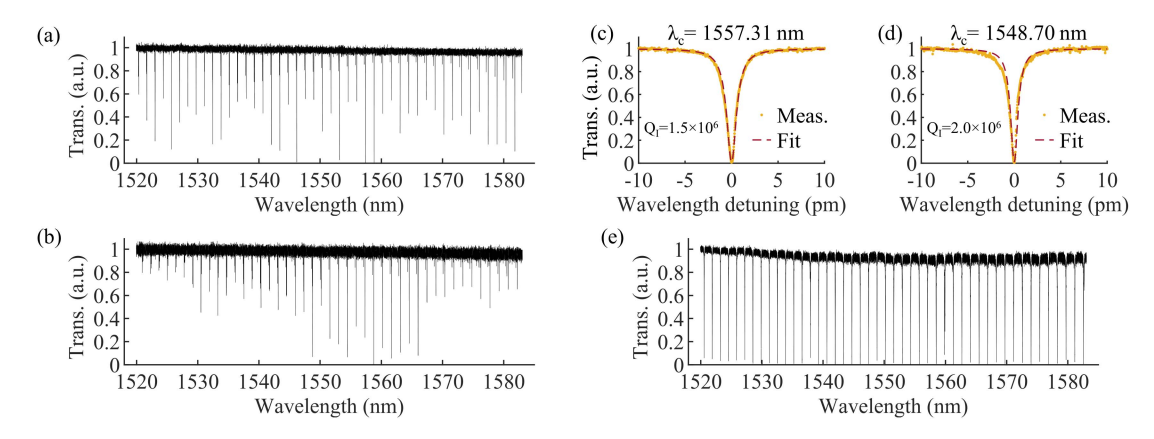


Fig. 6. Transmission response of SiO_x clad (a) ring and (b) disc resonators. Zoomed in transmission response of the (c) ring and (d) disc resonances at 1557.31 and 1548.70 nm respectively. Transmission response of (e) S1813 coated ring resonator.

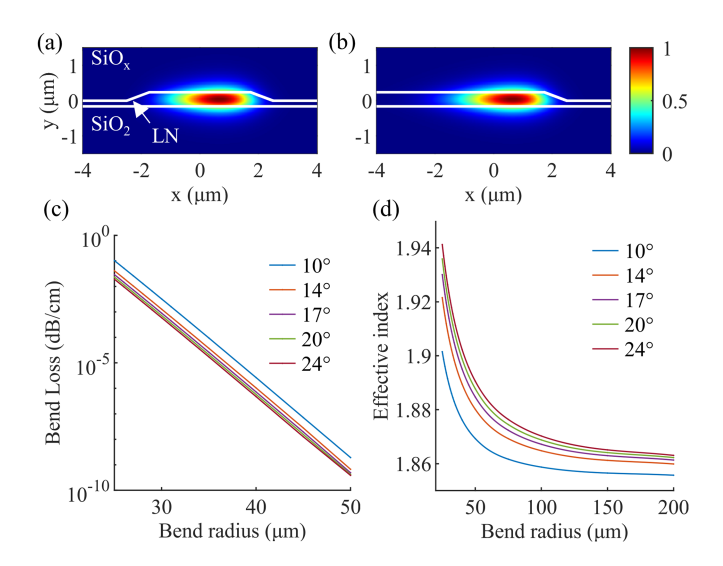


Fig. 7. Simulated quasi- TE_0 optical mode profiles ($|E_x|$) of (a) ring (waveguide base width = 5 μ m) and (b) disk resonators of radius 150 μ m at 1550 nm. Simulated (c) excess bending loss and (d) mode effective index of quasi- TE_0 mode at 1550 nm for different sidewall angles and bending radii for a ring resonator with 5 μ m base waveguide, 240 nm rib height, and 400 nm LN film thickness.

exceeding 1100 °C may be required to significantly reduce (by 87%) hydrogen impurity concentration in $\mathrm{SiO_x}$ deposited using PECVD [51]. However, annealing at these high temperatures cannot be implemented on our devices since temperatures of more than 600 °C are observed to cause damage.

The rib sidewall angles demonstrated are shallow, however, they do not significantly contribute to the bending loss of our resonators as shown by electromagnetic simulations using finite difference method in Fig. 7. Simulated first order quasi-TE mode profiles plotting the magnitude of the transverse electric field ($|E_{\rm x}|$) in the bent ring and disc resonators of radius 150 μ m are shown in Fig. 7(a, b). Ring resonators with bending radii as small as 30 μ m may be fabricated with acceptable excess bend loss as shown in Fig. 7(c). Simulated effective indices in Fig. 7(d) also show that the effective index of the bent mode approaches that

of the straight waveguide for large radii but increases for small radii implying higher mode confinement towards the periphery of the resonators.

V. SUMMARY AND CONCLUSION

We demonstrate the fabrication of thin film LNOI microresonators exhibiting intrinsic and loaded Q factors of over one million using 405 nm photolithography and a PR reflow method suitable for etching smooth LN rib waveguides through physical Ar sputtering. Reflowing the PR at temperatures greatly exceeding its glass transition temperature reduces sidewall surface roughness and increases etching resistance allowing it to be used both as the pattern mask and the hard etch mask. Waveguide sidewall surfaces with rms roughness as low as 0.49 nm are obtained using Ar plasma etching. Propagation losses of 0.11 dB/cm are demonstrated in the infrared C-band telecom range. Dependence of sidewall angle and sidewall surface roughness on waveguide width is characterized and the effects of thermal annealing on the propagation loss of silicon oxide cladded waveguides are also investigated. Fabricated devices exhibit a large thermal budget, allowing them to be heated up to 550 °C, useful for tuning or biasing, nonlinear optical or electro-optic devices respectively. Simulated bending loss suggests that the propagation loss of the fabricated ring resonators approaches that of a straight waveguide.

LNOI microresonators with Q factors of one million have been used to demonstrate highly efficient nonlinear optical processes [1], [10], while low loss rib waveguides find use in high performance electro-optic modulators [5], [6]. PR reflow may also be applied to other photonic platforms such as SiN, InP, SiC, and GaN which also benefit from low loss integrated waveguides and high Q factor microresonators. Additionally, the reflowed PR etch mask may exhibit a similar polishing resistance to that of SiO₂ [40], suggesting that the etch mask preparation method may also be used to pattern waveguides using CMP without requiring an additional hard mask layer, further simplifying the existing PLACE method.

REFERENCES

- J. Lu et al., "Periodically poled thin-film lithium niobate microring resonators with a second-harmonic generation efficiency of 250,000%/W,"
 Optica, vol. 6, no. 12, pp. 1455–1460, Dec. 2019, doi: 10.1364/OP-TICA.6.001455.
- [2] J.-Y. Chen, C. Tang, Z.-H. Ma, Z. Li, Y. M. Sua, and Y.-P. Huang, "Efficient and highly tunable second-harmonic generation in Z-cut periodically poled lithium niobate nanowaveguides," *Opt. Lett.*, vol. 45, no. 13, pp. 3789–3792, Jul. 2020, doi: 10.1364/OL.393445.
- [3] A. Rao, K. Abdelsalam, T. Sjaardema, A. Honardoost, G. F. Camacho-Gonzalez, and S. Fathpour, "Actively-monitored periodic-poling in thin-film lithium niobate photonic waveguides with ultrahigh nonlinear conversion efficiency of 4600%W⁻¹ cm⁻²," *Opt. Exp.*, vol. 27, no. 18, pp. 25920–25930, Sep. 2019, doi: 10.1364/OE.27.025920.
- [4] X. Ji et al., "Ultra-low-loss on-chip resonators with sub-milliwatt parametric oscillation threshold," *Optica*, vol. 4, no. 6, pp. 619–624, Jun. 2017, doi: 10.1364/OPTICA.4.000619.
- [5] C. Wang et al., "Integrated lithium niobate electro-optic modulators operating at CMOS-compatible voltages," *Nature*, vol. 562, no. 7725, pp. 101–104, Oct. 2018, doi: 10.1038/s41586-018-0551-y.
- [6] M. Xu et al., "High-performance coherent optical modulators based on thin-film lithium niobate platform," *Nature Commun.*, vol. 11, no. 1, Aug. 2020, Art. no. 3911, doi: 10.1038/s41467-020-17806-0.
- [7] O. T. Celik et al., "High-bandwidth CMOS-voltage-level electro-optic modulation of 780 nm light in thin-film lithium niobate," Opt. Exp., vol. 30, no. 13, pp. 23177–23186, Jun. 2022, doi: 10.1364/OE.460119.
- [8] G.-T. Xue et al., "Ultrabright multiplexed energy-time-entangled photon generation from lithium niobate on insulator chip," *Phys. Rev. Appl.*, vol. 15, no. 6, Jun. 2021, Art. no. 064059, doi: 10.1103/PhysRevApplied.15.064059.
- [9] J. Zhao, C. Ma, M. Rüsing, and S. Mookherjea, "High quality entangled photon pair generation in periodically poled thin-film lithium niobate waveguides," *Phys. Rev. Lett.*, vol. 124, no. 16, Apr. 2020, Art. no. 163603, doi: 10.1103/PhysRevLett.124.163603.
- [10] J. Lu, M. Li, C. L. Zou, A. A. Sayem, and H. X. Tang, "Toward 1% single-photon anharmonicity with periodically poled lithium niobate microring resonators," *Optica*, vol. 7, no. 12, pp. 1654–1659, Dec. 2020, doi: 10.1364/OPTICA.403931.
- [11] M. Zhang et al., "Broadband electro-optic frequency comb generation in a lithium niobate microring resonator," *Nature*, vol. 568, no. 7752, pp. 373–377, Apr. 2019, doi: 10.1038/s41586-019-1008-7.
- [12] A. Shams-Ansari et al., "Thin-film lithium-niobate electro-optic platform for spectrally tailored dual-comb spectroscopy," *Commun. Phys.*, vol. 5, no. 1, Apr. 2022, Art. no. 88, doi: 10.1038/s42005-022-00865-8.
- [13] M. Leidinger, S. Fieberg, N. Waasem, F. Kühnemann, K. Buse, and I. Breunig, "Comparative study on three highly sensitive absorption measurement techniques characterizing lithium niobate over its entire transparent spectral range," *Opt. Exp.*, vol. 23, no. 17, pp. 21690–21705, Aug. 2015, doi: 10.1364/OE.23.021690.
- [14] K. Prabhakar, R. J. Patton, and R. M. Reano, "Stress reduction and wafer bow accommodation for the fabrication of thin film lithium niobate on oxidized silicon," *J. Vac. Sci. Technol. B*, vol. 39, no. 6, Dec. 2021, Art. no. 062208, doi: 10.1116/6.0001283.
- [15] L. Chen, J. Nagy, and R. M. Reano, "Patterned ion-sliced lithium niobate for hybrid photonic integration on silicon," *Opt. Mater. Exp.*, vol. 6, no. 7, pp. 2460–2467, Jul. 2016, doi: 10.1364/OME.6.002460.
- [16] P. Rabiei, J. Ma, S. Khan, J. Chiles, and S. Fathpour, "Heterogeneous lithium niobate photonics on silicon substrates," *Opt. Exp.*, vol. 21, no. 21, pp. 25573–25581, Oct. 2013, doi: 10.1364/OE.21.025573.
- [17] A. N. R. Ahmed, S. Shi, M. Zablocki, P. Yao, and D. W. Prather, "Tunable hybrid silicon nitride and thin-film lithium niobate electrooptic microresonator," *Opt. Lett.*, vol. 44, no. 3, pp. 618–621, Feb. 2019, doi: 10.1364/OL.44.000618.
- [18] M. V. Kotlyar, S. Iadanza, and L. O'Faolain, "Lithium niobate Fabry-Perot microcavity based on strip loaded waveguides," *Photon. Nanostructures Fundam. Appl.*, vol. 43, Feb. 2021, Art. no. 100886, doi: 10.1016/j.photonics.2020.100886.
- [19] X. Huang, Y. Liu, Z. Li, Z. Fan, and W. Han, "High-performance and compact integrated photonics platform based on silicon rich nitride– lithium niobate on insulator," *APL Photon.*, vol. 6, no. 11, Nov. 2021, Art. no. 116102, doi: 10.1063/5.0065437.
- [20] H. Hu, R. Ricken, W. Sohler, and R. B. Wehrspohn, "Lithium niobate ridge waveguides fabricated by wet etching," *IEEE Photon. Technol. Lett.*, vol. 19, no. 6, pp. 417–419, Mar. 2007, doi: 10.1109/LPT.2007.892886.

- [21] J. Lin, F. Bo, Y. Cheng, and J. Xu, "Advances in on-chip photonic devices based on lithium niobate on insulator," *Photon. Res.*, vol. 8, no. 12, pp. 1910–1936, Dec. 2020, doi: 10.1364/PRJ.395305.
- [22] M. Zhang, C. Wang, R. Cheng, A. Shams-Ansari, and M. Lončar, "Mono-lithic ultra-high-Q lithium niobate microring resonator," *Optica*, vol. 4, no. 12, pp. 1536–1537, Dec. 2017, doi: 10.1364/OPTICA.4.001536.
- [23] C. Wang et al., "Integrated high quality factor lithium niobate microdisk resonators," *Opt. Exp.*, vol. 22, no. 25, pp. 30924–30933, Dec. 2014, doi: 10.1364/OE.22.030924.
- [24] J. Lin et al., "Fabrication of high-Q lithium niobate microresonators using femtosecond laser micromachining," *Sci. Rep.*, vol. 5, no. 1, Jan. 2015, Art. no. 8072, doi: 10.1038/srep08072.
- [25] R. Wu et al., "Long low-loss-litium niobate on insulator waveguides with sub-nanometer surface roughness," *Nanomaterials*, vol. 8, no. 11, Nov. 2018, Art. no. 910, doi: 10.3390/nano8110910.
- [26] J. Zhang et al., "Fabrication of crystalline microresonators of high quality factors with a controllable wedge angle on lithium niobate on insulator," *Nanomaterials*, vol. 9, no. 9, Sep. 2019, Art. no. 1218, doi: 10.3390/nano9091218.
- [27] R. Wolf, I. Breunig, H. Zappe, and K. Buse, "Scattering-loss reduction of ridge waveguides by sidewall polishing," *Opt. Exp.*, vol. 26, no. 16, pp. 19815–19820, Aug. 2018, doi: 10.1364/OE.26.019815.
- [28] J. Zhou et al., "Electro-optically switchable optical true delay lines of meter-scale lengths fabricated on lithium niobate on insulator using photolithography assisted chemo-mechanical etching," *Chin. Phys. Lett.*, vol. 37, no. 8, Jul. 2020, Art. no. 084201, doi: 10.1088/0256-307X/37/8/084201.
- [29] Y. Liang et al., "Monolithically integrated electro-optic modulator fabricated on lithium niobate on insulator by photolithography assisted chemo-mechanical etching," *J. Phys. Photon.*, vol. 3, no. 3, Jul. 2021, Art. no. 034019, doi: 10.1088/2515-7647/ac0cc0.
- [30] J. Zhang et al., "High-index-contrast single-mode optical waveguides fabricated on lithium niobate by photolithography assisted chemo-mechanical etching (PLACE)," *Jpn. J. Appl. Phys.*, vol. 59, no. 8, Jul. 2020, Art. no. 086503, doi: 10.35848/1347-4065/aba0d6.
- [31] M. Shen et al., "Etch planarization A new approach to correct non-uniformity post chemical mechanical polishing," in *Proc. 25th Annu. SEMI Adv. Semicond. Manuf. Conf.*, 2014, pp. 423–427. doi: 10.1109/ASMC.2014.6846968.
- [32] K. Luke, P. Kharel, C. Reimer, L. He, M. Loncar, and M. Zhang, "Wafer-scale low-loss lithium niobate photonic integrated circuits," *Opt. Exp.*, vol. 28, no. 17, pp. 24452–24458, Aug. 2020, doi: 10.1364/OE.401959.
- [33] K. Zhang, Z. Chen, H. Feng, W.-H. Wong, E. Y.-B. Pun, and C. Wang, "High-Q lithium niobate microring resonators using liftoff metallic masks," *Chin. Opt. Lett.*, vol. 19, no. 6, Jun. 2021, Art. no. 060010.
- [34] G. A. Porkolab, P. Apiratikul, B. Wang, S. H. Guo, and C. J. K. Richardson, "Low propagation loss AlGaAs waveguides fabricated with plasma-assisted photoresist reflow," *Opt. Exp.*, vol. 22, no. 7, pp. 7733–7743, Apr. 2014, doi: 10.1364/OE.22.007733.
- [35] F. T. O'Neill and J. T. Sheridan, "Photoresist reflow method of microlens production Part I: Background and experiments," *Optik*, vol. 113, no. 9, pp. 391–404, Jan. 2002, doi: 10.1078/0030-4026-00186.
- [36] A. Boes, L. Chang, T. Nguyen, G. Ren, J. Bowers, and A. Mitchell, "Efficient second harmonic generation in lithium niobate on insulator waveguides and its pitfalls," *J. Phys. Photon.*, vol. 3, no. 1, Jan. 2021, Art. no. 012008, doi: 10.1088/2515-7647/abd23a.
- [37] S. Ranganathan, R. McCreery, S. M. Majji, and M. Madou, "Photoresist-Derived carbon for microelectromechanical systems and electrochemical applications," *J. Electrochem. Soc.*, vol. 147, no. 1, 2000, Art. no. 277, doi: 10.1149/1.1393188.
- [38] R. Lum, C. W. Wilkins, M. Robbins, A. M. Lyons, and R. P. Jones, "Thermal analysis of graphite and carbon-phenolic composites by pyrolysis-mass spectrometry," *Carbon*, vol. 21, no. 2, pp. 111–116, Jan. 1983, doi: 10.1016/0008-6223(83)90165-3.
- [39] A. Singh, J. Jayaram, M. Madou, and S. Akbar, "Pyrolysis of negative photoresists to fabricate carbon structures for microelectromechanical systems and electrochemical applications," *J. Electrochem. Soc.*, vol. 149, no. 3, 2002, Art. no. E78, doi: 10.1149/1.1436085.
- [40] A. Itoh, M. Imai, and Y. Arimoto, "Photoresist chemical mechanical polishing for shallow trench isolation," *Jpn. J. Appl. Phys.*, vol. 37, no. 4R, Apr. 1998, Art. no. 1697, doi: 10.1143/JJAP.37.1697.
- [41] P. G. de Gennes, "Wetting: Statics and dynamics," Rev. Mod. Phys., vol. 57, no. 3, pp. 827–863, Jul. 1985, doi: 10.1103/RevModPhys.57.827.

- [42] A. C. Muir, S. Mailis, and R. W. Eason, "Ultraviolet laser-induced submicron spatially resolved superhydrophilicity on single crystal lithium niobate surfaces," *J. Appl. Phys.*, vol. 101, no. 10, May 2007, Art. no. 104916, doi: 10.1063/1.2734539.
- [43] R. J. Good and M. N. Koo, "The effect of drop size on contact angle," *J. Colloid Interface Sci.*, vol. 71, no. 2, pp. 283–292, Sep. 1979, doi: 10.1016/0021-9797(79)90239-X.
- [44] S. Xiao, M. H. Khan, H. Shen, and M. Qi, "Modeling and measurement of losses in silicon-on-insulator resonators and bends," *Opt. Exp.*, vol. 15, no. 17, pp. 10553–10561, Aug. 2007, doi: 10.1364/OE.15.010553.
- [45] H.-J. Schliwinski, U. Schnakenberg, W. Windbracke, H. Neff, and P. Lange, "Thermal annealing effects on the mechanical properties of plasma-enhanced chemical vapor deposited silicon oxide films," *J. Electrochem. Soc.*, vol. 139, no. 6, Jun. 1992, Art. no. 1730, doi: 10.1149/1.2069484.
- [46] J. Fu, H. Shang, Z. Li, W. Wang, and D. Chen, "Thermal annealing effects on the stress stability in silicon dioxide films grown by plasmaenhanced chemical vapor deposition," *Microsystem Technol.*, vol. 23, no. 7, pp. 2753–2757, Jul. 2017, doi: 10.1007/s00542-016-3005-1.

- [47] B. G. Lee, A. Biberman, P. Dong, M. Lipson, and K. Bergman, "All-optical comb switch for multiwavelength message routing in silicon photonic networks," *IEEE Photon. Technol. Lett.*, vol. 20, no. 10, pp. 767–769, May 2008, doi: 10.1109/LPT.2008.921100.
- [48] R. D. Mansoor, H. Sasse, M. A. Asadi, S. J. Ison, and A. P. Duffy, "Over coupled ring resonator-based add/drop filters," *IEEE J. Quantum Electron.*, vol. 50, no. 8, pp. 598–604, Aug. 2014, doi: 10.1109/JQE.2014.2329645.
- [49] Q. Li, Z. Zhang, J. Wang, M. Qiu, and Y. Su, "Fast light in silicon ring resonator with resonance-splitting," *Opt. Exp.*, vol. 17, no. 2, pp. 933–940, Jan. 2009. doi: 10.1364/OE.17.000933.
- [50] M. Bahadoran and I. S. Amiri, "Double critical coupled ring resonator-based add-drop filters," *J. Theor. Appl. Phys.*, vol. 13, no. 3, pp. 213–220, Sep. 2019, doi: 10.1007/s40094-019-00343-7.
- [51] C. K. Wong, H. Wong, M. Chan, C. W. Kok, and H. P. Chan, "Fabrication of optical waveguide using silicon oxynitride prepared by thermal oxidation of silicon rich silicon nitride," in *Proc. IEEE Conf. Electron Devices Solid-State Circuits*, 2005, pp. 471–474. doi: 10.1109/EDSSC.2005.1635310.